ORIGINAL RESEARCH

Imaging Cerebral Arteries Tortuosity and Velocities by Transcranial Doppler Ultrasound Is a Reliable Assessment of Brain Aneurysm in Mouse Models

Héloïse Lebas, PhD; Alexandre Boutigny, MD,[#]; Clémence Maupu, MS,[#]; Jonas Salfati, BS; Cyrille Orset, PhD; Mikael Mazighi, MD, PhD; Philippe Bonnin, MD, PhD; Yacine Boulaftali, PhD [ID]

BACKGROUND: During the past few decades, several pathophysiological processes contributing to intracranial aneurysm (IA) rupture have been identified, including irregular IA shape, altered hemodynamic stress within the IA, and vessel wall inflammation. The use of preclinical models of IA and imaging tools is paramount to better understand the underlying disease mechanisms.

METHODS: We used 2 established mouse models of IA, and we analyzed the progression of the IA by magnetic resonance imaging, transcranial Doppler, and histology.

RESULTS: In both models of IA, we observed, by transcranial Doppler, a significant decrease of the blood velocities and wall shear stress of the internal carotid arteries. We also observed the formation of tortuous arteries in both models that were correlated with the presence of an aneurysm as confirmed by magnetic resonance imaging and histology. A high grade of tortuosity is associated with a significant decrease of the mean blood flow velocities and a greater artery dilation.

CONCLUSIONS: Transcranial Doppler is a robust and convenient imaging method to evaluate the progression of IA. Detection of decreased blood flow velocities and increased tortuosity can be used as reliable indicators of IA.

Key Words: animal models ■ arterial tortuosity ■ intracranial aneurysms ■ ultrasound Doppler

Intracranial aneurysms (IAs) are pathological focal dilatations of intracranial arteries mainly located on the circle of Willis. Their rupture, occurring in 6 per 100 000 persons, has severe consequences including death in 27% to 44% of patients.[1] Risk factors contributing to the formation of IA include hypertension, smoking, family history of IA, head trauma, or female sex.[1] During the past decade, several patho-physiological processes involved in the development and rupture of IAs have been identified, such as inflammation or altered hemodynamic characteristics. Abnormal blood flow plays a key role in IA development and localization, commonly found at arterial bifurcations where excessive hemodynamic stresses are exerted on arterial walls.[2] There is a close relationship between wall shear stress (WSS), endothelial dysfunction, and

downstream inflammation.[3] WSS, defined as the frictional force tangent to vessel wall induced by blood flow, is an important hemodynamic parameter. High and low WSS play a role in the formation and progression of IA.[4] In particular, high shear stress has been reported to modify the local expression of several other genes that contribute to IA formation, including matrix metalloproteinases and tissue inhibitors of matrix metalloproteinases, within the aneurysm wall.[5] In patients, hemodynamic parameters are mainly studied by computational fluid dynamics calculated on high resolution data sets such as 3-dimensional digital subtraction angiography. Recently, computational fluid dynamics on high-resolution 9.4T magnetic resonance imaging (MRI) data sets has been performed to image the circle of Willis in mice.[6] However, this high-field MRI is not readily available in preclinical research. Existing mouse models for IA require a tedious histological analysis to study pathophysiological mechanisms involved in aneurysm formation.[7–9] Therefore, there is a need for a convenient and reliable imaging technique to study IA formation and hemodynamic alteration in intracranial arteries of mice. In this study, we used transcranial Doppler (TCD) imaging to evaluate IA formation and progression by monitoring arterial tortuosity and blood flow velocities in intracranial arteries of 2 well-known mouse models of IA.

Nonstandard Acronyms and Abbreviations

ACA   anterior cerebral artery
IA   intracranial aneurysm
ICA   internal carotid artery
mBFVel mean blood flow velocity
TCD   transcranial Doppler
WSS   wall shear stress

CLINICAL PERSPECTIVE

- Transcranial Doppler is a fast, robust, and noninvasive novel imaging modality to monitor intracranial aneurysm formation and development in mouse models. Transcranial Doppler reveals arterial tortuosity and measures hemodynamic alterations, key features of intracranial aneurysm pathophysiology.

- Until now, hemodynamic alterations, a main feature of human intracranial aneurysms, are poorly studied in mouse models because of technical limits. Here, we provide a new imaging method to quantify hemodynamic parameters such as the mean blood flow velocity and wall shear stress, which allow us to monitor the development of intracranial aneurysms. Our work may contribute significantly to how the field can study the underlying mechanisms of this disease.

METHODS

The data that support the findings of this study are available from the corresponding author on reasonable request.

Mice

C57BL6 mice were bred and housed in our local conventional animal facility. All experiments were performed in accordance with French ethical laws (agreement number animal protocol n°3962) and conformed to the Animal Research: Reporting of In Vivo Experiments 2.0 guidelines. All animals were maintained under standard conditions and kept on a 12-hour light/dark cycle with food and water given ad libitum (maximum 5 animals per cage).

IA Induction

IAs were induced as described by Nuki et al and Hosaka et al in 8- to 10-week-old C57BL6 mice.[7,9] Control animals (8- to 10-week-old C57BL6 mice) received no surgical procedure or hypertension induction. We previously assessed the arterial tortuosity, blood flow velocity, and arterial diameter in control mice and mice subjected to chronic hypertension induced by a subcutaneous implantation of an osmotic pump (ALZET 2004) filled with angiotensin II (1000 ng/kg per minute), and no difference was observed.

Briefly, in the Hosaka et al model, chronic hypertension is induced via right renal artery and left common carotid artery ligations in deeply anesthetized female mice (n=23). One week later, stereotaxic injection (coordinates: 1.2 rostral, 0.7 lateral, 6 mm deep) of elastase (1 U/mL diluted in 10 μL of saline solution) was performed, followed by subcutaneous implantation of an osmotic pump (ALZET 2004) filled with angiotensin II (1000 ng/kg per minute). In addition, β-aminopropionitrile was delivered in drinking water (0.12%, Sigma–Aldrich) throughout the model (Figure 1A). Control mice were 8- to 10-week-old C57BL6 female mice (n=7).

The Nuki et al model consists of a stereotaxic injection in the right basal cistern (coordinates: 2.5 posterior,
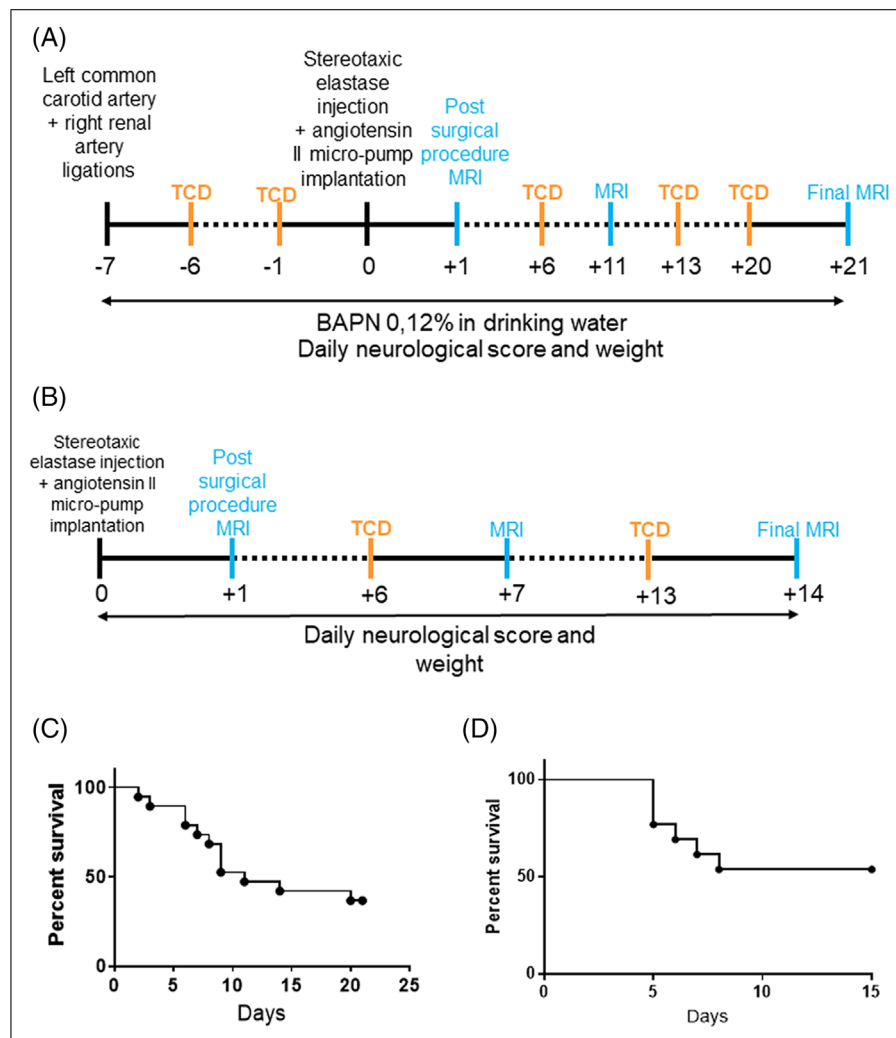
FIGURE 1. General overview of IA models. Schematic time course of the Hosaka et al (**A**) and Nuki et al (**B**) models. TCD imaging and MRI are performed once a week, and the surgical procedure is detailed in the Methods section. Survival curve of mice subjected to the Hosaka et al (n=23) (**C**) or Nuki et al (n=14) (**D**) model. IA indicates intracranial aneurysm; MRI, magnetic resonance imaging; and TCD, transcranial Doppler.

2.5 lateral, 6 mm deep) of 2.5 μL of elastase (35 mU diluted in saline solution) in deeply anesthetized male animals (n=14), followed by subcutaneous implantation of an osmotic pump (ALZET 2004) filled with angiotensin II (600 ng/kg per minute, Sigma–Aldrich) (Figure 1B). Control mice were 8- to 10-week-old male C57BL6 mice (n=13).

For each model, MRI was performed the day following elastase injection to exclude animals exhibiting an intracranial hemorrhage attributed to the surgical procedure. Once a week, each animal was scanned by MRI, and intracranial blood flow velocity was assessed by TCD. Animals were observed daily to monitor humane end point manifestation defined as weight loss (2 g in 24 hours) or onset of neurologic symptoms attributed to IA rupture.

For the Hosaka et al model, 4 mice were excluded after the elastase injection as a result of intracranial hemorrhage the day following the surgery, 5 mice were excluded during the course of the model as a result of thoracic or abdominal hemorrhage, 7 were euthanized because of humane end point manifestation, and 7 reached the end of the protocol (Supporting Information Figure S1). In the Nuki et al model, 1 mouse was excluded after the elastase injection because of intracranial hemorrhage the day following the surgery, 6 mice were euthanized as a result of humane end point manifestation, and 7 reached the end of the protocol (Supporting Information Figure S2).

Because of the variability observed in in vivo experiments and a survival rate of 30% and 50%, respectively, for the models by Hosaka et al and Nuki et al, a group size of ≈15 to 20 animals per model was determined by power analysis (2-sided, 2-sample t test, power=0.8, α=0.5, standard deviation ≈3) as optimal for determining statistical significance. Because no drug

was tested in this study, no randomization protocol was established. However, mice were anonymized throughout the study, particularly during MRI and ultrasound Doppler imaging, and analysis.

Magnetic Resonance Imaging

MRI images were acquired in a blinded manner on a Pharmascan 7T/12 cm system using surface coils (Brucker, Germany). During acquisition, anesthesia of thermoregulated mice was maintained using isoflurane 1.5%. T2∗-weighted sequences were acquired using a fast, low-angle shot sequence and used to detect intracranial hemorrhage in hyposignal. A 3-dimensional T1-weighted sequence was performed to visualize IA as an abnormal dilation of intracranial arteries.

Transcranial Ultrasound Doppler

A blinded operator performed ultrasound measurements on thermoregulated mice under isoflurane anesthesia (1.0%) using an echocardiograph (ACUSON SEQUOIA, Siemens, Erlangen, Germany) equipped with a 14.5-MHz linear transducer. The transducer was placed at the back of the head and neck allowing a horizontal cross-sectional view of the base of the skull. The color-coded Doppler then drew the circle of Willis (the pulsed repetition frequency was set to 7813 Hz). The Doppler sample of the pulsed Doppler was placed successively in the left and right internal carotid arteries (ICAs) in the left and right anterior and posterior cerebral arteries and then in the basilar trunk for Doppler velocity waveform recordings (Doppler sample wide was set to 0.5 mm, and the pulsed repetition frequency was set between 12 500 and 15 625 Hz). Spectral analysis of the Doppler velocity waveforms was recorded at different time points in each model of IA. Time-averaged, spatial-averaged mean blood flow velocities (mBFVels) were then measured after Doppler beam longitudinal axis of the artery angle correction (every time $<\pm10°$ angle correction was used with the cross-sectional view used to perform blood flow recordings in all studied arteries). Heart rates were recorded to ensure the absence of cardiorespiratory depression during mBFVel acquisitions. The mBFVel measurements were previously investigated in control mice at basal states for intraobserver repeatability. Two series of measurements separated by a 10-minute interval were recorded in 10 mice. The repeatability coefficient (RC) was calculated based on ISO 5725 that is, according to the formula $RC^2 = \Sigma Di^2/n$, where Di is the relative (positive or negative) difference within each pair of measurements, and n is the sample. The intraobserver repeatability coefficient values were 0.3, 0.4, 0.4, and 0.4 cm/s for ICA, anterior cerebral artery (ACA), posterior cerebral artery, and basilar trunk, respectively, largely inferior to the differences exhibited between the different values recorded at the different time points. Differences were then considered significant.

Histology

Each mouse was deeply anesthetized and transcardially perfused with saline (25 mL) followed by 20 mL of fixative solution (0.5% zinc chloride, 0.5% zinc acetate in 0.1 M Tris base buffer containing 0.05% calcium acetate, pH 7.4). Brains were postfixed with zinc fixative solution (48 hours, 4°C) and paraffin embedded, and microtome transversal sections (10 μm) were collected and stained with orcein to visualize the arterial elastic lamina.

Analysis

All analyses and TCD image grading were performed in a blinded manner. TCD image grade scale is based on apparent tortuosity of the circle of Willis arteries: grade 0 indicates normal appearing arteries compared with healthy animals (and retrograde blood flow in left ICA and ACA in the Hosaka et al model), grade 1 indicates slight tortuosity (1 curvature), grade 2 indicates pronounced tortuosity (3 curvatures), and grade 3 indicates advanced tortuosity (4 curvatures and more). The 4 grades were identified in the Hosaka et al model, but only grades 0 and 1 were observed in the Nuki et al model.

WSS was calculated according to the formula WSS$=\mu\times((8\times mBFVel)/D)$ in dynes/cm^2,[10] where μ is dynamic blood viscosity (0.04 g/cm per s) and D is the diameter of the vessel measured on MRI 3-dimensional T1-weighted images.[11]

Statistical Analysis

Results are represented as mean±95% CI. Data and statistical processing were performed with GraphPad Prism 7 software. We assessed all data distribution through the D'Agostino and Pearson normality test. For parametric analysis, differences between multiple groups were analyzed by 1-way ANOVA followed by a Tukey's multiple comparison test. For nonparametric data, statistical significance across groups defined by 1 factor was performed using the Kruskal–Wallis test followed by a nonparametric t test (Mann–Whitney test). The level of statistical significance was set at $P<0.05$. Unless indicated, nonparametric tests were used. To assess correlations, the Spearman correlation was calculated.

RESULTS

To study the usefulness of TCD imaging in the detection of brain aneurysms, we employed 2 mouse models of cerebral aneurysm described in the literature, respectively, referred to as the models by Hosaka et al and Nuki et al.[7,9]

IA Imaging by TCD and MRI in the Mouse Model by Hosaka et al

In control mice, an anterograde cerebral blood flow (in red on TCD images) originating from the left and right ICA mainly supply the left and right ACA, respectively (Figure 2A). A retrograde blood flow (appearing in blue on TCD images) originating from both the ICA and the basilar trunk supplies the bilateral posterior cerebral arteries (Figure 2A). All arteries analyzed by MRI presented with a straight shape and a homogeneous diameter. Moreover, analysis of the histological staining showed an intense and continuous orcein staining of the elastic lamina.

In mice subjected to the Hosaka et al model, 1 day after left common carotid artery ligation, we observed by TCD the rerouting of the cerebral blood flow in the circle of Willis. The left ICA and ACA were supplied via a retrograde blood flow originating from the anterior azygos cerebral artery (equivalent to the anterior communicant artery in human) (Figure 2A, grade 0). This ligation was associated with a stereotaxic elastase injection in hypertensive mice and led to the development of intracranial arterial tortuosity on the right ICA and ACA observed in both TCD and MRI (Figure 2A; grades 1, 2, and 3, yellow arrows). Furthermore, this tortuosity was associated with IA formation characterized by elastic lamina disruption and degradation and artery dilation (Figure 2A; grades 2 and 3). Six days before elastase injection and hypertension induction (day −6), all mice were scored as grade 0 and as early as day −1, 75% of mice presented a grade 1 tortuosity (Figure 2B). From days 6 to 20 (following elastase injection and hypertension induction), mice presenting a grade 2 tortuosity increased from 46% to 57%, and grade 3 tortuosity increased from 6% to 28% (Figure 2B). By day 21, 76.9% of animals developed an IA and 38% survived (Figure 1C).

As a result of the left ICA ligation, a marked increase of the mBFVel in the right ICA was measured after the surgery in grade 0 compared with control mice, from 13.5 ± 0.8 cm/s to 22.4 ± 1.6 cm/s ($P<0.01$; Figure 3A). Increased mBFVel was maintained in grade 1 mice (24.1 ± 1.3 cm/s), but significantly decreased in grades 2 and 3 mice compared with grades 0 and 1 mice (18.6 ± 1.3 cm/s; $P<0.05$; Figure 3A). Moreover, the correlation between the mBFVel and the right ICA diame-
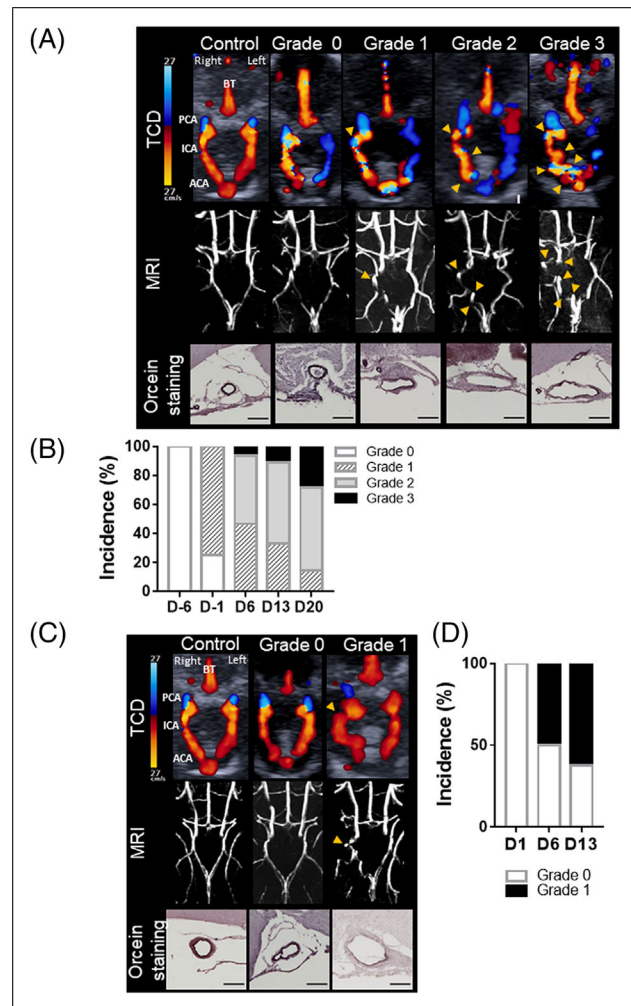

FIGURE 2. Increased arterial tortuosity detected by TCD imaging and confirmed by MRI uncover intracranial aneurysm formation. Schematic representation of intracranial arteries. Representative TCD and T1-weighted MRI images of control and grades 0, 1, 2, and 3 mice subjected to the models by Hosaka et al (**A**) and Nuki et al (**C**) and the corresponding representative orcein staining of the right ICA (deep purple, elastic lamina; scale bar: 100 μm). Arrowheads indicate abnormal curvatures. Percentage of apparent tortuous arteries, on TCD images, within the circle of Willis during the course of the Hosaka et al model (**B**) and Nuki et al model (**D**). ACA indicates anterior cerebral artery; BT, basilar trunk; D, day; ICA, internal carotid artery; MRI, magnetic resonance imaging; PCA, posterior cerebral artery; and TCD, transcranial Doppler.

ter measured by MRI showed a significant correlation ($R2$, 0.405; $P=0.0013$; Figure 3C). Mice with a high tortuosity grade (grades 2 and 3, orange dots) presented with a more severe artery dilation and mBFVel decrease than grade 1 (blue dots) and grade 0 mice (gray dots). Because of the increased mBFVel induced by the left common carotid artery ligation, the WSS significantly increased in the right ICA of grade 0 mice compared with control mice (control, 158.1 ± 8.4 dynes/cm^2; grade 0, 241.5 ± 12.5 dynes/cm^2; $P<0.001$; Figure 3E).
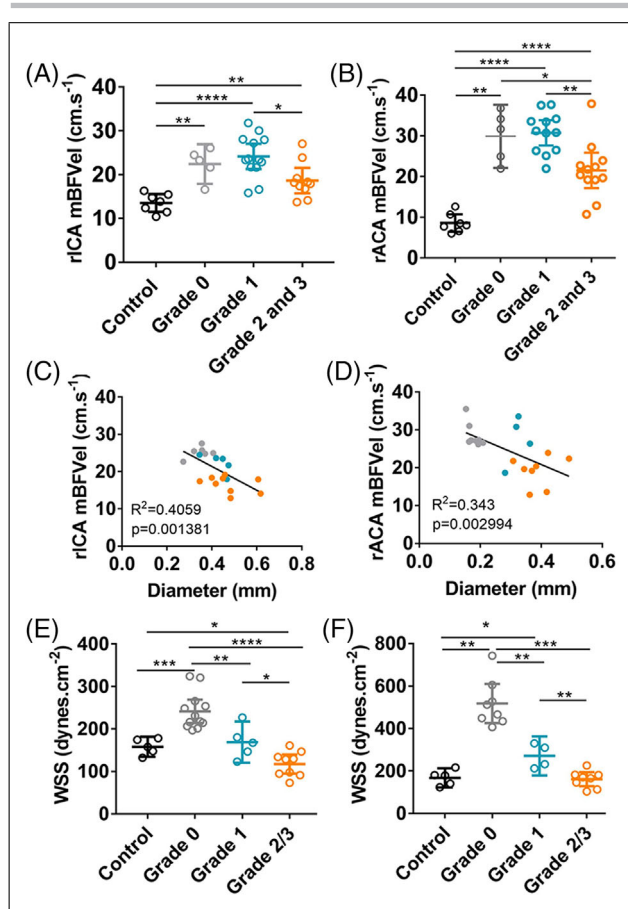
FIGURE 3. Hemodynamic parameters are altered in highly tortuous intracranial arteries in the Hosaka et al model. A and **B**, Measurements of the mBFVel in the rICA or rACA by transcranial Doppler of control mice (n=7) and mice subjected to the Hosaka et al model (n=23). **C** and **D**, Correlation between the mBFVel and rICA or rACA diameter measured by magnetic resonance imaging (gray, grade 0; blue, grade 1; orange, grades 2/3). **E** and **F**, Calculated WSS in the rICA or rACA of control mice and mice subjected to the Hosaka et al model according to their tortuosity grade. Data are represented as mean±95% CI. Kruskal–Wallis test followed by Mann–Whitney test has been used except for (**A**), where a 1 ANOVA followed by Tukey's posttest was carried out. $*P<0.05$, $**P<0.01$, $***P<0.001$, and $****P<0.0001$. mBFVel indicates mean blood flow velocity; rACA, right anterior cerebral artery; rICA, right internal carotid artery; and WSS, wall shear stress.

However, we observed that the higher the mice were graded for their arterial tortuosity, the lower their calculated WSS was (grade 1, 169±17.4 dynes/cm^2; grades 2 and 3, 117.4±9.7 dynes/cm^2; $P<0.05$; Figure 3E).

Similarly, in the right ACA, where arterial tortuosity is observed (Figure 2A; grades 2 and 3), mBFVel increased in grades 0 and 1 mice compared with control mice (control, 8.5±0.8 cm/s versus grade 0, 29.8±2.7 cm/s and grade 1, 30.7±1.4 cm/s [$P<0.01$ and $P<0.001$, respectively]) and was significantly decreased in grades 2 and 3 mice compared with lower grades (grades 2 and 3, 21.5±1.9 cm/s;

$P<0.01$; Figure 3B). As for the right ICA, there was a significant correlation between the mBFVel and the right ACA diameter ($R^2 = 0.343$; $P=0.0029$; Figure 3D), and the calculated WSS significantly decreased as the tortuosity grade increased (grade 0, 518±38.9 dynes/cm^2; grade 1, 271.2±28.8 dynes/cm^2; grades 2 and 3, 161.4±14 dynes/cm^2; $P<0.01$; Figure 3F).

IA Imaging by TCD and MRI in the Mouse Model by Nuki et al

In mice subjected to the Nuki et al model, stereotaxic elastase injection in conjunction with angiotensin-II induced hypertension led to the development of ICA tortuosity, as determined by TCD imaging and confirmed through MRI (Figure 2C, yellow arrows). This apparent tortuosity was associated with altered vessel wall integrity characterized by elastic lamina degradation and arterial dilation (Figure 2C, grade 1 orcein staining). From days 6 to 13, mice presenting with grade 1 tortuosity increased from 50% to 62.5% (Figure 2D). At the conclusion of the Nuki et al protocol, 66% of animals developed an IA and 53% survived (Figure 1D).

In the right ICA, the mBFVel was significantly decreased in grade 0 mice compared with control mice (13.1±0.8 cm/s versus 18±0.6 cm/s; $P<0.01$; Figure 4A). The mBFVel was further reduced in grade 1 mice (presenting with arterial tortuosity on TCD and MRI images) compared with control and grade 0 mice (grade 1, 8.9±0.8 cm/s; $P<0.01$; Figure 4A). In addition, there was a significant correlation between the right ICA mBFVel and its diameter, as measured by MRI (R^2, 0.472; $P=0.006$; Figure 4C). As in the Hosaka et al model, we observed that mice with arterial tortuosity (grade 1, orange dots) present with more severe artery dilation and decreased mBFVel than grade 0 (blue dots) and control mice (gray dots) (Figure 4C). Furthermore, the calculated WSS was significantly decreased in grades 0 and 1 mice compared with controls (grade 0, 110.6±4.3 dynes/cm^2; and grade 1, 83.5±8.7 dynes/cm^2 versus control, 206.3±16.7 dynes/cm^2 [$P<0.01$ and $P<0.001$, respectively]) and was significantly further decreased in grade 1 mice compared with grade 0 mice (Figure 4E).

Decreased mBFVel in the right ACA was also observed in grade 0 and grade 1 mice compared with control mice (grade 0, 9.1±0.7 cm/s and grade 1, 7.3±0.7 cm/s versus control, 11.9±0.8 cm/s [$P<0.05$ and $P<0.001$, respectively]; Figure 4B). Interestingly, in agreement with the absence of apparent tortuosity on the right ACA on TCD and MRI images, no difference of mBFVel was observed between grades 0 and 1 mice (Figure 4B). MRI and TCD data showed no correlation between the mBFVel and the arterial diameter for the right ACA (R^2, 0.110; $P=0.09$; Figure 4D). In addition,
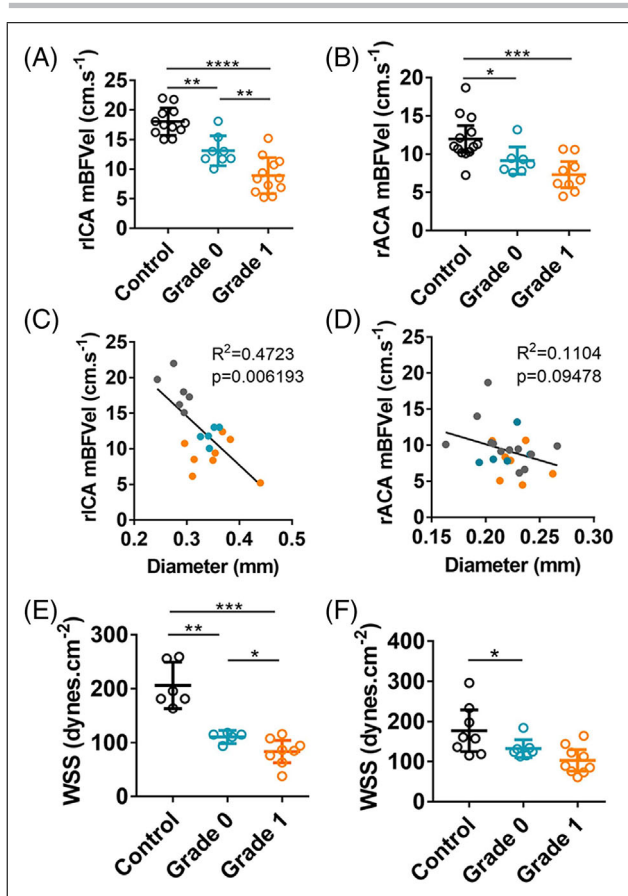
FIGURE 4. Hemodynamic parameters are altered in tortuous intracranial arteries in the Nuki et al model. A and **B**, Comparison of the mBFVel, measured by transcranial Doppler, in the rICA or rACA of control mice (n=12) and mice subjected to the Nuki et al model (n= 14) according to their tortuosity grade. **C** and **D**, Correlation between mBFVel and rICA or rACA diameter measured by magnetic resonance imaging (gray, control; blue, grade 0; orange, grade 1). **E** and **F**, Calculated WSS in the rICA or rACA of control mice and mice subjected to the Nuki et al model according to tortuosity grade. Data are represented as mean±95% CI. Kruskal–Wallis test followed by a Mann–Whitney test has been used. $*P<0.05$, $**P<0.01$, $***P<0.001$, and $****P<0.0001$. mBFVel indicates mean blood flow velocity; rACA, right anterior cerebral artery; rICA, right internal carotid artery; and WSS, wall shear stress.

there was no difference between the calculated WSS of grade 0 and grade 1 mice (respectively, 132.8±9 dynes/cm^2 and 103.4±11.6 dynes/cm^2; Figure 4F).

DISCUSSION

The gold standard to image brain aneurysms in preclinical models is based on MRI followed by histological analysis to confirm IA formation in animal models. MRI imaging is expensive, time consuming, and not readily available. In addition, it requires specific postprocedure imaging software to visualize the brain vasculature.

Here, we use the ultrasound imaging as a novel method to longitudinally study IA formation in mice.

Doppler ultrasound imaging is a widely used technique to monitor vessel blood flow in different aneurysm animal models, namely, thoracic and abdominal aneurysms, as reviewed in Ito et al.[12] To our knowledge, our study is the first to describe the use of TCD in brain aneurysms. There are several models of IA used in large animals (pigs, dogs, and rabbits) or small animals (rodents). In mice, there are 3 main models: (1) the Morimoto et al model, which describes aneurysm formation at the site of the ACA and olfactory artery bifurcation (the main limitations of this model are the time frame of aneurysm formation [>4 months] and their very small size [arterial wall protrusion of a few micrometers]); (2) the Nuki et al model based on a stereotaxic elastase injection in hypertensive mice that allows for the study of IA formation; and (3) the Hosaka et al model, which is a combination of the 2 aforementioned models, including the ligation of the left common carotid and the right renal arteries before the elastase injection in hypertensive mice. This model allows the study of the aneurysm formation and rupture.

In the models by Nuki et al and Hosaka et al, we demonstrate that the presence of arterial tortuosity is significantly correlated with the presence of an aneurysm, as confirmed by MRI and histological analyses. We also demonstrate that a high grade of tortuosity is associated with a significant decrease in the mBFVels of the ICAs and increased arterial dilation. In light of our findings, it is tempting to speculate whether that tortuosity could be a proxy for aneurysm growth and/or rupture. In the Hosaka et al model, we observed that the appearance of tortuosity precedes the injection of elastase, whereas in the Nuki et al model, tortuosity and aneurysm appear simultaneously. In both models, IA always appears after elastase injection and after the appearance of tortuosity. Based on our experience, tortuosity requires the induction of hypertension and/or β-aminopropionitrile (BAPN) administration. It is only after the injection of elastase that we observed dilation of the artery. Accordingly, patients with high ICA tortuosity present with IA.[13,14] Moreover, patients with high arterial tortuosity display lower WSS, which can promote matrix metalloproteinase activation, weakening of the arterial wall,[15] and leukocyte infiltration.[16] Clinical and experimental studies strongly suggest that mechanical factors such as blood pressure, blood flow, axial tension, and structural changes in the vessel wall play important roles in the development of arterial tortuosity.[17] In addition, computational studies have shown that luminal shear stress and wall stress are altered in tortuous arteries.[18,19] Nevertheless, the molecular mechanisms governing arterial tortuosity remain unknown.

High shear stress has been clearly shown to contribute to cerebral aneurysm formation.[4,20] However, there is still a debate about whether high shear stress or low shear stress contributes to the rupture. The high shear stress hypothesis states that the increase of WSS triggers endothelial dysfunction, vascular wall remodeling, and degeneration.[4,20] Similarly, low shear stress can contribute to the accumulation of blood cells (red blood cells, platelets, and leukocytes) at the site of an aneurysm, leading to the weakening of the aneurysm wall and the rupture.[4,20] Experimental computational fluid dynamics analysis shows that the WSS is lower in the aneurysm region compared with the vessel region, suggesting that high shear stress initiates the aneurysm formation and the low shear stress rather facilitates the growth and subsequently the rupture of the aneurysm.[21] In line with these observations, our data show that at the site of an aneurysm with high tortuosity grade, the WSS is significantly lower compared with an aneurysm with low tortuosity grade.

In mice as well as in humans, alteration of blood flow velocities plays a key role in the modulating arterial diameter.[22] Previous studies have shown that an increase in blood velocities induces an outward physiological adaptation of the vascular wall.[23] In the Morimoto et al model,[8] induced by arterial ligation in nonhypertensive mice, small vascular protrusions characterized by some fragmentations of the internal elastic lamina are formed in several months, which may reflect a slow remodeling process. To the contrary, in the models by Nuki et al and Hosaka et al,[7,9] the arterial wall degradation induced by the elastase and hypertension contribute to the accelerated dilation and the formation of tortuous aneurysms, highlighting a pathological outward remodeling rather than a growth of the arterial wall. Lower blood flow velocities and WSS, as observed in both models, have been shown to induce the expression of proinflammatory molecules[24] and the release of vasoactive molecules by endothelial cells and smooth muscle cells.[22,25] The recruitment of leukocytes to the diseased artery and altered vascular tone are key components in the outward remodeling.[7,26]

We contend that TCD may represent a promising new imaging technique for IA in animal models, however, limitations exist. Indeed, TCD imaging fails to detect IA located on circle of Willis branches, such as the middle cerebral artery, despite the IA presence confirmed through MRI and histology. Moreover, arterial diameter cannot be accurately measured on TCD images as the spatial resolution of the TCD modifies the apparent artery diameter. By TCD imaging, we can detect aneurysms because of the measure of decreased blood flow velocity (ranging from 12 to 19 cm/s for the right ICA in the Hosaka et al model), which was significantly correlated with the increased diameter measured by MRI (ranging from 0.35 to 0.60 mm for the right ICA in the Hosaka et al model). Nevertheless, a feature of the technique is that we cannot detect the early phase of an aneurysm by TCD as it has been described by electron microscopy in the Morimoto et al model.[8]

Our work shows, for the first time, the advantage of TCD as a complementary method to image and follow the progression of brain aneurysms in preclinical models. Our findings provide a rationale for assessing the tortuosity and the drop of the intracranial blood flow velocity to predict IA severity in mice. The TCD imaging method can be used to study pathophysiological mechanisms leading to aneurysm formation and progression.

REFERENCES

1. Etminan N, Chang HS, Hackenberg K, de Rooij NK, Vergouwen MDI, Rinkel GJE, Algra A. Worldwide incidence of aneurysmal subarachnoid hemorrhage according to region, time period, blood pressure, and smoking prevalence in the population: a systematic review and meta-analysis. *JAMA Neurol*. 2019;76:588-597. https://doi.org/10.1001/jamaneurol.2019.0006
2. Kondo S, Hashimoto N, Kikuchi H, Hazama F, Nagata I, Kataoka H. Cerebral aneurysms arising at nonbranching sites. an experimental study.

Stroke. 1997;28:398-403; discussion 403–404. https://doi.org/10.1161/01.str.28.2.398

3. Nixon AM, Gunel M, Sumpio BE. The critical role of hemodynamics in the development of cerebral vascular disease. *J Neurosurg*. 2010;112:1240-1253. https://doi.org/10.3171/2009.10.JNS09759

4. Soldozy S, Norat P, Elsarrag M, Chatrath A, Costello JS, Sokolowski JD, Tvrdik P, Kalani MYS, Park MS. The biophysical role of hemodynamics in the pathogenesis of cerebral aneurysm formation and rupture. *Neurosurg Focus*. 2019;47:E11. https://doi.org/10.3171/2019.4.FOCUS19232.

5. Kadirvel R, Ding YH, Dai D, Zakaria H, Robertson AM, Danielson MA, Lewis DA, Cloft HJ, Kallmes DF. The influence of hemodynamic forces on biomarkers in the walls of elastase-induced aneurysms in rabbits. *Neuroradiology*. 2007;49:1041-1053. https://doi.org/10.1007/s00234-007-0295-0

6. Tutino VM, Rajabzadeh-Oghaz H, Chandra AR, Gutierrez LC, Schweser F, Preda M, Chien A, Vakharia K, Ionita C, Siddiqui A, Kolega J. 9.4T magnetic resonance imaging of the mouse circle of willis enables serial characterization of flow-induced vascular remodeling by computational fluid dynamics. *Curr Neurovasc Res*. 2018;15:312-325. https://doi.org/10.2174/1567202616666181127165943

7. Hosaka K, Downes DP, Nowicki KW, Hoh BL. Modified murine intracranial aneurysm model: aneurysm formation and rupture by elastase and hypertension. *J Neurointerv Surg*. 2014;6:474-479. https://doi.org/10.1136/neurintsurg-2013-010788

8. Morimoto M, Miyamoto S, Mizoguchi A, Kume N, Kita T, Hashimoto N. Mouse model of cerebral aneurysm: experimental induction by renal hypertension and local hemodynamic changes. *Stroke*. 2002;33:1911-1915. https://doi.org/10.1161/01.STR.0000021000.19637.3D

9. Nuki Y, Tsou TL, Kurihara C, Kanematsu M, Kanematsu Y, Hashimoto T. Elastase-induced intracranial aneurysms in hypertensive mice. *Hypertension*. 2009;54:1337-1344. https://doi.org/10.1161/HYPERTENSIONAHA.109.138297

10. Roux E, Bougaran P, Dufourcq P, Couffinhal T. Fluid shear stress sensing by the endothelial layer. *Front Physiol*. 2020;11:861. https://doi.org/10.3389/fphys.2020.00861

11. Greve JM, Les AS, Tang BT, Draney Blomme MT, Wilson NM, Dalman RL, Pelc NJ, Taylor CA. Allometric scaling of wall shear stress from mice to humans: quantification using cine phase-contrast MRI and computational fluid dynamics. *Am J Physiol Heart Circ Physiol*. 2006;291:H1700-H1708. https://doi.org/10.1152/ajpheart.00274.2006

12. Ito S, Lu HS, Daugherty A, Sawada H. Imaging techniques for aortic aneurysms and dissections in mice: comparisons of ex vivo, in situ, and ultrasound approaches. *Biomolecules*. 2022;12:339. https://doi.org/10.3390/biom12020339

13. Kliś KM, Krzyżewski RM, Kwinta BM, Stachura K, Gąsowski J. Tortuosity of the internal carotid artery and its clinical significance in the development of aneurysms. *J Clin Med*. 2019;8:E237. https://doi.org/10.3390/jcm8020237

14. Labeyrie PE, Braud F, Gakuba C, Gaberel T, Orset C, Goulay R, Emery E, Courthéoux P, Touzé E. Cervical artery tortuosity is associated with intracranial aneurysm. *Int J Stroke*. 2017;12:549-552. https://doi.org/10.1177/1747493016687577

15. Zhang J, Liu Q, Han HC. An in vivo rat model of artery buckling for studying wall remodeling. *Ann Biomed Eng*. 2014;42:1658-1667. https://doi.org/10.1007/s10439-014-1017-5

16. Godin D, Ivan E, Johnson C, Magid R, Galis ZS. Remodeling of carotid artery is associated with increased expression of matrix metalloproteinases in mouse blood flow cessation model. *Circulation*. 2000;102:2861-2866. https://doi.org/10.1161/01.cir.102.23.2861

17. Han HC. Twisted blood vessels: symptoms, etiology and biomechanical mechanisms. *J Vasc Res*. 2012;49:185-197. https://doi.org/10.1159/000335123

18. Qiao AK, Guo XL, Wu SG, Zeng YJ, Xu XH. Numerical study of nonlinear pulsatile flow in S-shaped curved arteries. *Med Eng Phys*. 2004;26:545-552. https://doi.org/10.1016/j.medengphy.2004.04.008

19. Kaplan AD, Jaffa AJ, Timor IE, Elad D. Hemodynamic analysis of arterial blood flow in the coiled umbilical cord. *Reprod Sci*. 2010;17:258-268. https://doi.org/10.1177/1933719109351596

20. Sforza DM, Putman CM, Cebral JR. Hemodynamics of cerebral aneurysms. *Annu Rev Fluid Mech*. 2009;41:91-107. https://doi.org/10.1146/annurev.fluid.40.111406.102126

21. Shojima M, Oshima M, Takagi K, Torii R, Hayakawa M, Katada K, Morita A, Kirino T. Magnitude and role of wall shear stress on cerebral aneurysm: computational fluid dynamic study of 20 middle cerebral artery aneurysms. *Stroke*. 2004;35:2500-2505. https://doi.org/10.1161/01.STR.0000144648.89172.0f

22. Davies PF. Flow-mediated endothelial mechanotransduction. *Physiol Rev*. 1995;75:519-560. https://doi.org/10.1152/physrev.1995.75.3.519

23. Kamiya A, Togawa T. adaptive regulation of wall shear stress to flow change in the canine carotid artery. *Am J Physiol*. 1980;239:H14-H21. https://doi.org/10.1152/ajpheart.1980.239.1.H14

24. Zhao Y, Ren P, Li Q, Umar SA, Yang T, Dong Y, Yu F, Nie Y. Low shear stress upregulates CX3CR1 expression by inducing VCAM-1 via the NF-κb pathway in vascular endothelial cells. *Cell Biochem Biophys*. 2020;78:383-389. https://doi.org/10.1007/s12013-020-00931-4

25. Buus CL, Pourageaud F, Fazzi GE, Janssen G, Mulvany MJ, De Mey JG. Smooth muscle cell changes during flow-related remodeling of rat mesenteric resistance arteries. *Circ Res*. 2001;89:180-186. https://doi.org/10.1161/hh1401.093575

26. Bakker ENTP, Matlung HL, Bonta P, de Vries CJ, van Rooijen N, Vanbavel E. Blood flow-dependent arterial remodelling is facilitated by inflammation but directed by vascular tone. *Cardiovasc Res*. 2008;78:341-348. https://doi.org/10.1093/cvr/cvn050